International Journal of Rock Mechanics & Mining Sciences 169 (2023) 105418

Contents lists available at ScienceDirect

International Journal of Rock Mechanics and Mining Sciences

journal homepage: www.elsevier.com/locate/ijrmms

Investigation of coupled hydro-mechanical modelling of hydraulic fracture propagation and interaction with natural fractures

Yu Hu [a,b,*], Quan Gan [c,b,**], Andrew Hurst [b], Derek Elsworth [d]

[a] CNOOC Research Institute, Beijing, China
[b] Department of Geology and Geophysics, School of Geosciences, University of Aberdeen, UK
[c] College of Resources and Safety Engineering, Chongqing University, Chongqing, China
[d] Department of Energy and Mineral Engineering, EMS Energy Institute and G3 Center, Pennsylvania State University, University Park, PA, USA

ARTICLE INFO

Keywords:
Hydro-mechanical coupling
Hydraulic fracturing
Fracture propagation and interaction
Hydraulic fractures
Natural fractures
Fractured rock

ABSTRACT

Various fracture patterns may develop through hydraulic fracture propagation and interaction with natural fractures which may substantially enhance connectivity and connected fracture surface area in low-permeability formations. Key factors controlling this behavior are analyzed using the continuum simulator TOUGHREACT-FLAC3D that couples the evolution of stress and deformation (FLAC3D) with reactive fluid flow (TOUGHREACT) in fractured rock. The three potential interaction scenarios are accommodated - for the hydraulic fracture to directly cross, stay arrested by, or reinitiate from the intersected natural fracture. The results show that the combined effects of approach-angle and differential stress affect the normal closure response acting on fractures. Also, larger approach-angles, greater stress differences, and higher fracture shear strength favor direct crossing, with tensile stresses more readily transferred to the far-side of the approached natural fracture. Higher injection rates accelerate buildup of wellbore and fracture pressures which lead to more rapid propagation of the hydraulic fracture. Higher injection rates also increase the wellbore pressure and pressure gradient when injection rate exceeds leak-off rate of fractures arrested by the natural fracture. The presence of only single natural fractures results in faster hydraulic fracture propagation and greater propagation length driven by higher developed wellbore pressures than where dual natural fractures are present. The presence of dual parallel natural fractures hinders the propagation of the hydraulic fracture along its preferred original path as a result of greater and redistributed leak-off and diminution of pressure through the natural fractures. Increased natural fracture permeability slows hydraulic fracture propagation by increasing fluid flow and resulting pressure dissipation by the natural fractures. Combined, these factors influence mechanisms of fracture propagation and interaction, and evolution of flow paths, which are essential in design of hydraulic fracturing treatments, hydro-mechanical characterization and prediction of the response of stimulated fracture networks.

1. Introduction

1.1. Hydraulic fracture propagation and interaction

Hydraulic fracture propagation and interaction with natural fractures in low permeability rock matrix can greatly facilitate fluid recovery by enhancing the conductivity of fracture networks and shortening the length of effective drainage path across the rock. A hydraulic fracture will initiate when fluid overpressurization exceeds the concerted impediments of rock strength and in situ stress.[1] The originally expected fracture propagation direction may be influenced by local heterogeneity of rock properties, making the present-day orientation is often inconsistent with the orientation of natural fractures which are controlled by previous orientations of the in situ tectonic stress. Hence, the optimal orientation of propagating hydraulic fractures and the orientation of tectonically-induced natural fractures may intersect and crosscut each other and form complex fracture networks.

When the hydraulic fracture approaches and intersects with the natural fractures, classical interaction models and experiments[2–4] suggest that higher differential stress, approach-angles, and frictional coefficient may influence and favor crossing jointly. Analyses have been extended[5] for full range of approach-angles in brittle linear elastic

* Corresponding author. CNOOC Research Institute, Beijing, China.
** Corresponding author. College of Resources and Safety Engineering, Chongqing University, Chongqing, China.
E-mail addresses: yuhu1@foxmail.com, huyu7@cnooc.com.cn (Y. Hu).

https://doi.org/10.1016/j.ijrmms.2023.105418
Received 18 January 2022; Received in revised form 29 December 2022; Accepted 27 May 2023
1365-1609/© 2023 Elsevier Ltd. All rights reserved.

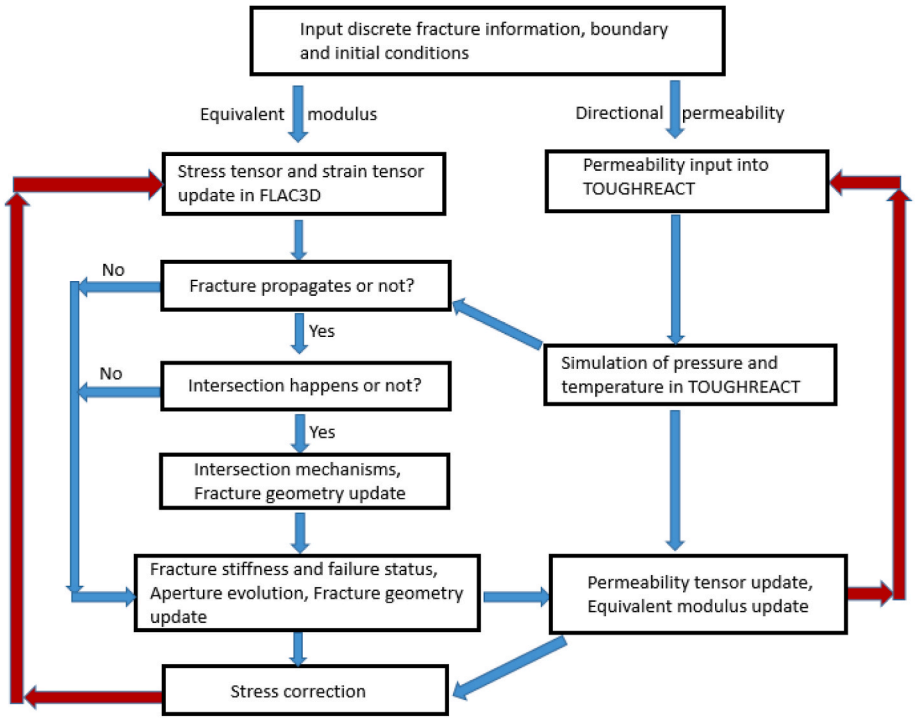

Fig. 1. Equivalent continuum simulation workflow implemented in TOUGHREACT-FLAC3D[46].

rocks.[6] Further extended analytical models include those accommodating a full range of approach-angles and cohesive natural interfaces.[7] Also, hydraulic fracture propagation in experiments have been demonstrated to follow the least resistant and shortest path to approach and interact with natural fractures.[8,9] Although analytical solutions and experimental studies are often limited by their assumptions, they provide a broad understanding of interaction mechanisms and may be enhanced by numerical modelling – less-constrained by limiting simplifications. More sophisticated experimental techniques, such as the monitoring of acoustic emission have also been implemented[10] in which a narrower natural fracture aperture resulted in an increase in the fracture fluid pressure for propagation and interaction - and consequently reduced production. Overall, experiments provide useful benchmarks and insight for the verification and investigation of fracture propagation and interaction mechanisms derived from analytical modelling and numerical studies.

1.2. Fluid flow in rock fractures

Understanding the hydraulic properties of rock fractures is important in understanding and modelling fluid flow through fractured rocks. Models of fluid flow through rock fractures can be characterized based on the traditional cubic law.[11] However, the traditional cubic law is applicable for Darcian flow and considered ubiquitous fracture aperture. Seepage analysis of the fracture network is based on fracture segments and intersections between fractures based on Darcy's flow. Seepage-pores fractal model was adopted in evaluation of coal permeability based on mercury porosimetry and Kozeny-Carman equation.[12] A dual-medium seepage model was also constructed[13] which considers water storage in fractures, stress, fracture length, and seepage pressure for seepage evolution. Another model of Darcian fluid flow within fractures which is derived from Snow's model[14] is considered accounting for the fluid exchange with matrix.[15] These models were based on the rationale of linear relationship between pressure drop and fluid flow rate. However, this rationale does not work for non-Darcian flow in which the Reynolds number exceeds critical values. In this situation, non-linear equations (e.g., nonlinear Navier-Stokes equations[16]) need to be calculated to accurately capture non-Darcian fluid flow in a rock fracture, which have been studied both theoretical and computational.[17,18]

1.3. Frameworks of simulation methods

The research of hydraulic fracture propagation and fracture interactions have been explored within continuum frameworks. Finite element modelling of fracture propagation and interaction typically requires various remeshing and non-remeshing strategies.[19–23] Extended finite element methods (XFEM) represent the presence of a discontinuity within an element without remeshing by enriching the degrees of freedom of that element by using displacement functions to represent fracture complexity.[24] Thus. fracture propagation in XFEM models is insensitive to mesh geometry,[25–27] however, these models can be computational demanding for large-scale problems.[28] The finite element code ABAQUS/Standard[30] embedded with its cohesive zone model[29] has been applied to hydraulic fracturing simulation with results matching those from both PKN[31,32] and KGD models.[33,34] Alternately, continuum approaches[35,36] may be adopted with ubiquitous joint constitutive models, as in TOUGHREACT-FLAC3D,[37,38] to represent the influence of natural fracture reactivation and slip due to fluid pressurization in enhanced geothermal systems. In addition, mixed-continuum embedded-fracture models[39] and PHF (permeability-based hydraulic fracture) models coupled through LSM (level set method)[28,40] have been shown to increase calculation efficiency in hydraulic fracturing by smearing fractures over the continuum without remeshing. A continuum-based combined finite-discrete element method (FDEM)[41] was developed, which is solid for the analysis of shear failure of fractures, whereas its implementation is difficult.

In comparison, discontinuum approaches assume that the rock mass consists of individual blocks delimited by explicit fractures[42] for better explicit representation of fracture deformations and block rotations. However, they can be computationally demanding for a large number of fractures or matrix blocks, more limited and suitable to simulate small-scale reservoirs in the short term[43] – due to their computational burden. In summary, the continuum approaches primarily assuming

Table 1
Summary of the primary governing equations.[46]

Fracture propagation criterion[49–52]	$K_{IC}^{*} \le K_I \le K_{IC}$
Stress correction considering the near-field solution in the K-field[72]	$\tilde{\boldsymbol{\sigma}}(\mathbf{x}) = \sum_{i=1}^{n_{gp}} \boldsymbol{\sigma}_i w_i A_i$
Fracture propagation incremental length	$l_{adv} = l_{\max}\left(\frac{G}{G_{\max}}\right)^{0.35}$
Fracture interaction criterion[3,27]	$\frac{-\sigma_n}{T_0 - \sigma_T} > \frac{\left(1 - \sin\frac{\theta}{2}\sin\frac{3\theta}{2}\right) + \frac{1}{\mu_f''\cos\frac{\theta}{2}}\left\lvert\sin\frac{\theta}{2}\cos\frac{\theta}{2}\cos\frac{3\theta}{2} + \alpha\right\rvert}{1 + \sin\frac{\theta}{2}\sin\frac{3\theta}{2}}$

continuum approaches can describe the macroscopic behavior of the fractured rock,[44] and significantly enhance the computational efficiency and are more suitable to represent large reservoir-scale fractured rock masses over extended duration[45] – the prime factor contributing to their utilization in this study.

In the following, we explore and analyze the key factors that influence hydraulic fracture propagation and interaction mechanisms in fractured rock masses, based on fracture propagation and interaction modules[46] developed specifically for the continuum simulator TOUGHREACT-FLAC3D.

2. Methodology

In equivalent continuum modeling, constitutive models are used to represent the rheology of the ensemble fractured rock mass – typically with a linearly-elastic matrix and with nonlinearly-inelastic fractures. The continuum simulator TOUGHREACT-FLAC3D couples fluid flow calculation (in TOUGHREACT)[47] with stress and deformation response (in FLAC3D).[48] The two programs are linked by a parsing code in FORTRAN, accommodating evolution of a stress-dependent fracture aperture and permeability tensor, stress intensity factor, energy release rate, fracture propagation criterion, stress correction around fracture tips, fracture propagation length, and fracture interaction criterion.

The stress intensity factor and energy release rate are calculated from fracture geometry and stress states, in order to quantify the tip energy, evaluate subcritical fracture propagation, and estimate propagation length. When hydraulic fractures approach and intersect natural fractures,[7] outcomes such as when the hydraulic fracture directly crosses, remains arrested by or reinitiates from natural fractures, add complexity for fracture patterns and analyses – and these are informed by principles of LEFM. These constitutive relationships provide a tractable solution to investigate mechanisms and factors that influence fracture propagation and interaction behaviors in rock masses. Some of the detailed methodology demonstrated in this section can be referred to Hu et al. (2021).[46]

Constitutive models for the evaluation of fracture propagation and interaction are developed in the coupling code accommodating the logic of Fig. 1. This logic allows the dynamic updating of permeability, stress, and modulus to be parsed between TOUGHREACT and FLAC3D as the solution proceeds.

2.1. Governing equations

The detailed explanation of the governing equations, including fracture propagation criterion, fracture propagation incremental length, fracture interaction criterion, etc., are presented in a previous associated paper (Hu et al. (2021)).[46]

The primary governing equations are summarized in Table 1, where K_I is the stress intensity factor; K_{IC} is the intrinsic fracture toughness of the intact material and $K_{IC}^{*} = 0.1K_{IC}$; $\tilde{\boldsymbol{\sigma}}$ is the weighted stress tensor in the element i after stress correction; l_{adv} is the fracture propagation

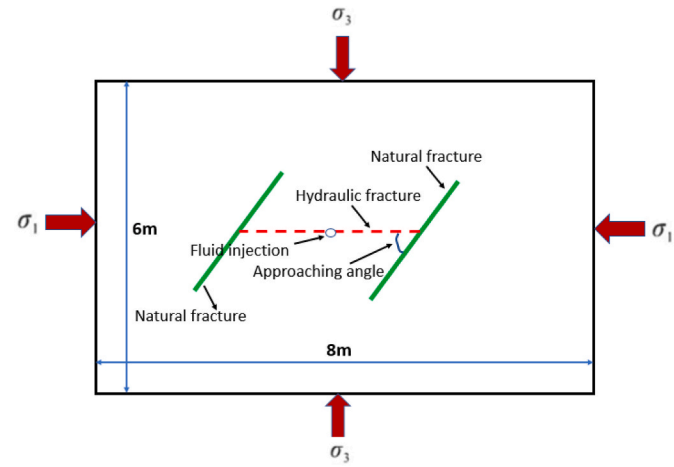

Fig. 2. Schematic of the model where a hydraulic fracture (dashed red line) approaching natural fractures (green lines)[46]. (For interpretation of the references to colour in this figure legend, the reader is referred to the Web version of this article.)

incremental length; l_{max} is the initial fracture length; G_{max} is the energy release rate G of the fracture tip which grows the fastest; θ is the approach angle; σ_T is the tangential stress of the fracture; T_0 is the tensile strength of the rock; α is the shear stress coefficient; μ_f'' is a calculated coefficient of friction of the natural fracture.

2.2. Fluid flow response in TOUGHREACT

Extension of Biot's poroelastic theory[54–57] is adopted in the dual-medium framework. The methodology represents the coupled stress-fluid flow response in the dual-medium model.

The basic equation which describes continuity of fluid mass is represented in a compressible media based on Darcy's law as,[58]

$$\frac{\partial \xi}{\partial t} - \frac{k}{\mu}\nabla^2 p = q \tag{1}$$

Eq. (1) combines Darcy's law for the flux term and provides a framework for flow-deformation response in a domain, where ξ is the increment of fluid content.[59]

Biot's (1941)[54] linear poroelastic constitutive equivalence for volumetric strain e is,

$$e = \frac{\sigma}{K} + \frac{p}{H} \tag{2}$$

$$\xi = \frac{\sigma}{H} + \frac{p}{R} \tag{3}$$

where $\frac{1}{K}$ is bulk drained compressibility; $\frac{1}{H}$ represents poroelastic expansion; $\frac{1}{R}$ represents specific storage.

The Skempton coefficient is calculated,

$$B = -\frac{\delta p}{\delta \sigma}\Big|_{\xi=0} = \frac{R}{H} \tag{4}$$

The Biot-Willis coefficient is,

$$\alpha = \frac{K}{H} \tag{5}$$

The specific storage is derived as,

$$\frac{1}{R} = -\frac{\delta \xi}{\delta p}\Big|_{\sigma=0} = \frac{\alpha}{KB} \tag{6}$$

Combining Eqs. (1)–(6) and extending to a dual-medium system, yields the flow condition for a dual-medium model[60] as,

Table 2
Initial properties of the model.[46]

Young's modulus (*GPa*)	8.4
Poisson's ratio	0.23
Initial fracture shear stiffness (*GPa/ m*)	500.0
Initial fracture normal stiffness (*GPa/ m*)	1300.0
Rock tensile strength (*MPa*)	3.73
Fracture cohesion (*MPa*)	0.5
Injection rate (*kg/s*)	0.0002
Fracture toughness ($MPa\sqrt{m}$)	1.5
Dilation angle (°)	3.0
Natural fracture friction angle (°)	20.81/41.67/50.42
Natural fracture friction coefficient	0.38/0.89/1.21
Natural fracture orientation (°)	30.0/60.0/90.0

$$\frac{k^{(i)}}{\mu}\nabla^2 p^{(i)} = \frac{\alpha^{(i)}}{K_u^{(i)}B^{(i)}}p^{(i)} + \alpha^{(i)}\dot{e} + (-1)^i\gamma\Delta p \tag{7}$$

Eq. (7) indicates a state of mass conservation, where i = 1 represents matrix medium; i = 2 represents fracture medium; B is the Skempton coefficient; $\dot{e}$ is the volumetric strain; p is the pressure; $\Delta p = (p_1 - p_2)$ is the instantaneous pressure differential;[61] γ is a coefficient for flow exchange for two domains;[62] α is the Biot-Willis coefficient; μ is the fluid viscosity; K_u is the undrained bulk modulus ($K_u \frac{\delta\sigma}{\delta\dot{e}}|_{\xi=0} = \frac{K}{1-\alpha B}$)

3. Verification

A model (Fig. 2) is constructed for numerical verification of hydraulic fracture propagation and interaction with natural fractures, against experimental results.[7,8] The model is 8 m × 6 m × 0.03 m in dimension[63] containing 2 m long natural fractures. Permeability of the natural fractures is defined as 100 mD.[64,65] The hydraulic fracture is assumed to initiate from a flaw length ($4 \times 10^{-3}m$) due to limitation of LEFM when representing fracture initiation. The initial simulation parameters are listed in Table 2.[7,44,63]

3.1. Numerical verification results

The numerical model is verified against experimental observations according to three different frictional angles and orientations of the natural fractures,[7,8,64] summarized in Table 3.

3.2. Analytical verification results

Also, analytical solution (Sneddon's solution) (Eq. (8)) is implemented for analytical verification as it can describe the linear model of hydraulic fracture propagation (Fig. 3) in which the fracture aperture *w* (x) under the plane strain condition with different maximum (S_H) and minimum principal stresses (S_h).

Properties of the analytical model are listed in Table 4.

The aperture of the hydraulic fracture is calculated as,

If $S_H \neq S_h$,

$$w(x) = \frac{4(1-\upsilon^2)}{E}\left[P_w - S_h + \frac{0.137\sqrt{R}}{[L+3(x-R)]^{1/1.3}}(S_H - S_h)\right]\sqrt{(L+R)^2 - x^2}$$
$$= \frac{4(1-0.23^2)}{8.3997\times 10^3}[4.6 - 3 + 0.123(13-3)]\sqrt{(0.169)^2 - 0.08^2} \approx 2.0\times 10^{-4}m \tag{8}$$

It shows that the analytical aperture result is reasonably close to the numerical aperture (2.5×10^{-4} m) result at the same location on the hydraulic fracture. Therefore, the numerical solution of the aperture can be relatively verified by the analytical solution.

In summary, the experimental and the numerical results match reasonably with a decent agreement except for several cases (Table 3) which may be caused by the heterogeneous and complex in situ tensile strength of the rock[67] as well as the limited experimental information of

Table 3
Tabulated verification results for the hydraulic fracture interacting with different friction and approaching angles of the natural fractures.[46]

Approaching angle (°)	σ_{max} (MPa)	σ_{min} (MPa)	Experimental results	Numerical results	
Internal friction angles of the natural fractures of 20.81°.					
90	8	3	Direct crossing	Direct crossing	
90	8	5	**Direct crossing**	**No direct crossing: staying arrested**	
60	10	3	**Direct crossing**	**No direct crossing: reinitiating**	
60	8	3	No direct crossing	No direct crossing: reinitiating	
30	10	3	No direct crossing	No direct crossing: reinitiating	
30	8	3	No direct crossing	No direct crossing: reinitiating	
Internal friction angles of the natural fractures of 41.67°.					
90	10	5	Direct crossing	Direct crossing	
90	10	3	Direct crossing	Direct crossing	
60	10	3	Direct crossing	Direct crossing	
60	13	3	Direct crossing	Direct crossing	
60	8	5	**No direct crossing**	**Direct crossing**	
30	10	5	No direct crossing	No direct crossing : staying arrested	
30	8	5	No direct crossing	No direct crossing: staying arrested	
30	13	3	No direct crossing	No direct crossing: reinitiating	
Internal friction angles of the natural fractures of 50.42°.					
90	8	3	**No direct crossing**	**Direct crossing**	
90	13	3	Direct crossing	Direct crossing	
60	13	3	**No direct crossing**	**Direct crossing**	
60	10	3	**No direct crossing**	**Direct crossing**	
30	13	3	No direct crossing	No direct crossing: reinitiating	
30	8	3	No direct crossing	No direct crossing: reinitiating	

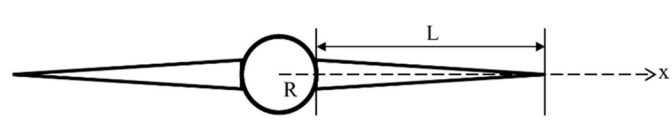

Fig. 3. Schematic of fracture propagation (enlarged for better figure view and not in realistic scale; modified from Zhang and Yin (2018))[66].

Table 4
Properties of the hydraulic fracture and rock mass for the analytical solution.

Maximum principal stress, S_H	13 MPa
Minimum principal stress, S_h	3 MPa
Poisson's ratio, ν	0.23
Young's modulus, E	8.3997×10^3 MPa
Wellbore pressure, P_w	4.6 MPa
L + R	0.169 m
R	0.002 m
x	0.08 m

Table 5
Tabulated results for different approach-angles (90°, 60°, and 30°) for a low coefficient of friction (Type I) of the natural fractures of 0.38.

Approaching angle (°)	σ_{max} (MPa)	σ_{min} (MPa)	Modelling results
90	8	3	Direct crossing
60	8	3	Reinitiating
30	8	3	Reinitiating

local stresses, rock properties and fracture treatment. The inconsistent comparison for high friction angle cases (50.42°) could be a result of the extra thickened material in the experiments which influences the mechanical properties of the media.[64] Also, the analytical result matches with the numerical solutions of the aperture of the hydraulic fracture reasonably. Considering the reasonable verification results for the majority of the cases, we continue investigating the behaviors of hydraulic fracture propagation and interaction with natural fractures in simple fracture systems for further parametric responses.

4. Analyses of fracture propagation and interaction

Hydraulic fracture propagation and their interaction with natural fractures are complex processes influenced by many factors including approach-angle, stress difference, friction angle, wellbore injection rate, natural fracture patterns and permeability, among others. A rectangular block (Fig. 2) represents a fractured rock mass.[63] We then explore the principal factors which control fracture propagation and interaction and the resulting mechanisms and fracture patterns from simulations based on the model (Table 3).

4.1. Effect of approach-angle

We compare the impacts of (Type I scenario) low, medium, and high approach-angles (30°, 60°, and 90°) between the hydraulic and natural fractures for a low friction coefficient of the natural fractures (0.38; Type I). These simulation results (Table 5; Fig. 4) show that the hydraulic fracture has a greater potential to cross the natural fractures directly when the approach-angle is high (approaching 90°). Furthermore, the

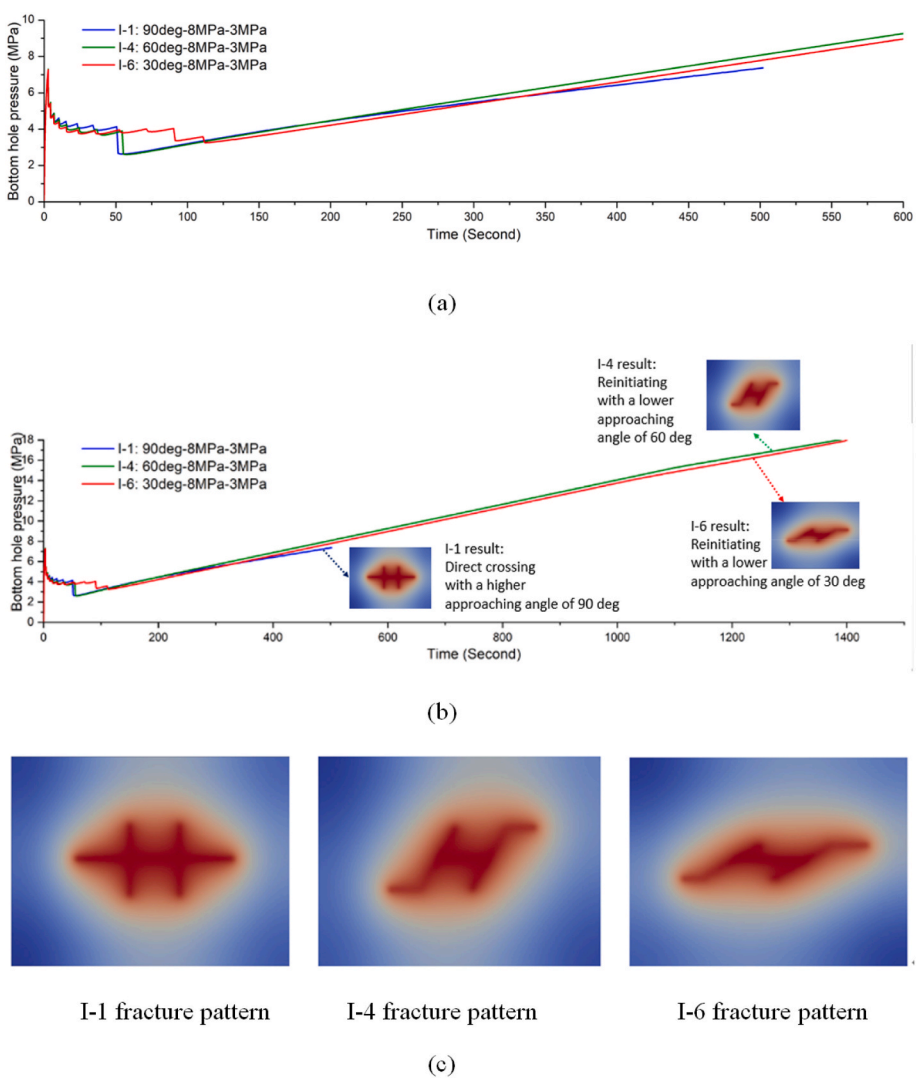

Fig. 4. Bottom hole pressure versus simulation time (a) zoomed-in segment for the first 600 s, and (b) the first 1400 s with simulation results for three different approach-angles compared: direct crossing with a high approach-angle of 90° (I-1), reinitiating with lower approach-angles of 90° (I-4) and 30° (I-6). Friction coefficient of the natural fractures is 0.38. The applied maximum and minimum principal stresses are 8 MPa and 3 MPa, respectively. (c). The zoomed-in results of I-1, I-4 and I-6 in (b).

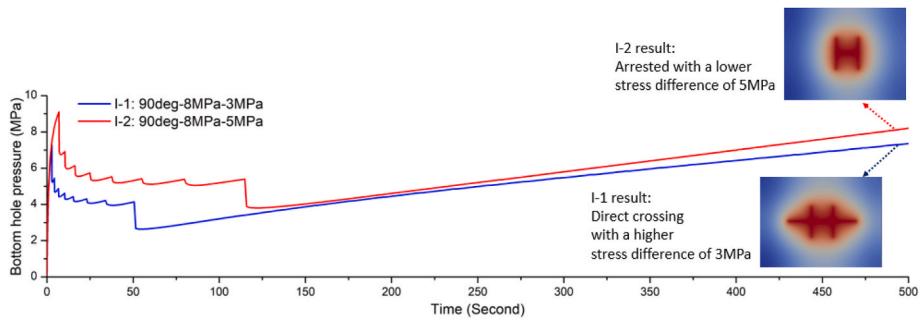

Fig. 5. Bottom hole pressure versus simulation time for different minimum principal stresses (3 MPa and 5 MPa) with a low friction coefficient (Type I). The maximum principal stress is 8 MPa. The friction coefficient is 0.38 (Type I). The approach-angle is 90°.

hydraulic fracture tends to reinitiate from the natural fractures for a low approach-angle (< 30°).

Fig. 4a indicates that the hydraulic fracture propagates faster for a larger approach-angle of 90° (I-1) than for a lower approach-angles of 60° and 30° (I-4 and I-6, respectively). In the early stages of propagation, following fracture initiation at ~6.2 MPa, wellbore pressure drops less when the approach-angle is higher – for example, a high approach-angle (I-1 for 90°) has a smaller wellbore pressure drop of ~1.7 MPa with the pressure reaching ~4.5 MPa, than for a low approach-angle (I-6 for 30°) which has a larger wellbore pressure drop of ~2.2 MPa with a pressure of ~4.0 MPa at ~20 s. This is because less fluid can leak-off into the natural fractures where the approach-angle is high. Higher approach-angles subject the natural fractures to higher compressive stresses from the applied stresses, resulting in greater normal closure of the natural fractures with less fluid leak-off. Subsequently, increased fluid supply increases driving pressures and promote hydraulic fracture propagation. Thus, the hydraulic fracture propagates faster with higher approach-angles (e.g., 90°) than lower approach-angles (e.g., 60° and 30°).

After intersection, if direct crossing occurs (e.g., the 90° I-1 case) then the hydraulic fracture propagates through to the other side of the natural fractures and extends the fluid flow path. Because of the small propagation increment, the rate of wellbore pressure increase exceeds the rate of pressure dissipation during the incremental propagation of the hydraulic fracture. Fig. 4b also illustrates that the wellbore pressure for the case of lower approach-angles (60° and 30°), where the hydraulic fracture cannot directly cross the natural fractures, and grows faster than the wellbore pressure for the high approach-angle case (90°) of direct crossing. These behaviors of increasing wellbore pressure are implied since the hydraulic fracture remains arrested at the location of intersection for an appreciable time without the possibility of reinitiating in the time range 0–600 s (Fig. 4a) for lower approach-angle cases (e.g., 30° and 60°). As a result, the wellbore pressures for the lower approach-angle cases of 30° and 60° (no direct crossing) increase faster (reaching ~8 MPa at 500 s) than the pressure for the high angle 90° (direct crossing) case (reaching ~7 MPa at 500 s). Hence, the wellbore pressure shows a faster increase for the lower approach-angle than the higher approach-angle after intersection between the hydraulic and natural fractures occurs.

In summary, the comparison indicates that crossing is more likely to occur with a high approach-angle, whereas the likelihood of the hydraulic fracture being arrested by, or later reinitiating from, the natural fracture increases when the approach-angle decreases. Also, the hydraulic fracture approaches the natural fractures faster when the approach-angles are higher. Any hydraulic fracture which directly crosses and continues propagating to the other side of the natural fracture will both dissipate and slow down the buildup of wellbore pressure.

4.2. *Effect of differential stress*

The effect of differential stress is investigated with two groups. In the first group, the maximum principal stress is kept constant at 8 MPa for a low friction coefficient of 0.38 (Type I) while the minimum principal stress is changed (Type I). In the second group the minimum principal stress is held constant at 3 MPa for a high friction coefficient of 1.21 (Type III) while the maximum principal stress is varied. The two scenarios are discussed separately below. Each group has an individual constant friction coefficient and the effect of differential stress (different minimum and maximum stresses, respectively) is compared within each group separately.

(1) Constant maximum principal stress

Fig. 5 indicates that fracture interaction behavior changes from directly crossing to arrested when the minimum principal stress increases from 3 MPa to 5 MPa. The approach-angle is 90° and the maximum applied stress is kept constant at 8 MPa.

Fig. 5 displays different interaction scenarios for a constant maximum principal stress of 8 MPa and minimum principal stresses of 3 MPa and 5 MPa. As a higher minimum principal stress requires higher pressures to induce fracture initiation and propagation, the higher minimum principal stress scenario of 5 MPa (I-2) yields higher fracture initiation and propagation pressures than the case for lower minimum principal stress at 3 MPa (I-1).

When the hydraulic fracture approaches the natural fractures, the near-tip stress field of the hydraulic fracture significantly enhances the

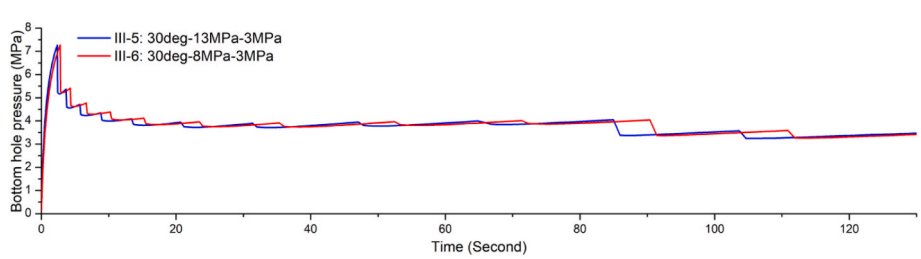

Fig. 6. Evolution of bottom hole pressure with time. Propagation at a larger differential stress (III-5) is compared with that for a smaller differential stress (III-6) for a constant minimum principal stress. The friction coefficient is 1.21 and the approach-angle is 30°.

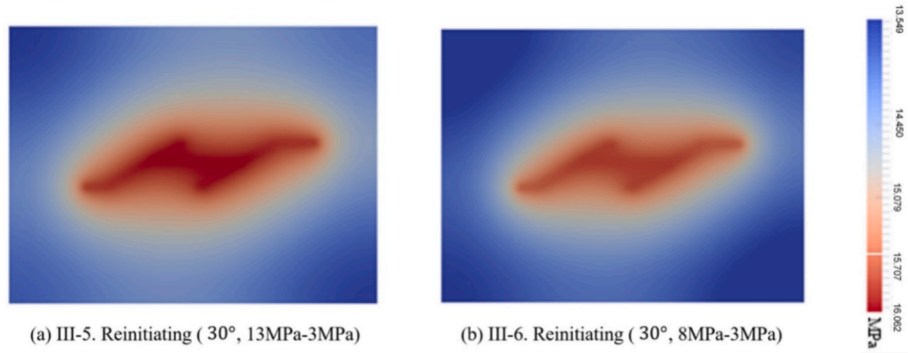

Fig. 7. Pressure distribution for different maximum principal stresses ((a) 13 MPa; (b) 8 MPa) at 1200 s. The minimum principal stress is 3 MPa for both scenarios. III-5 shows a higher fracture pressure relative to that in III-6.

fracture aperture through extensile strains. This results in a large pressure drop (~1.5 MPa) for I-1 at 50 s (Fig. 5). After the hydraulic fracture intersects the natural fracture, the hydraulic fracture continues to propagate due to the larger differential stress. The driven fracture directly crosses (I-1) the natural fractures to dissipate more pressure by transporting more fluid across the model, resulting in a slower buildup in wellbore pressure than if it remained arrested (e.g., I-1 has a smaller pressure of ~6 MPa relative to that of ~7.5 MPa for I-2 at 400 s).

Therefore, under constant maximum principal stress an elevated deviatoric stress initiates propagation of the fracture earlier and promotes faster propagation with a lower wellbore pressure. Such fractures tend to directly cross the natural fractures and continue extending and dissipating fluid. A smaller stress difference enhances the potential for the hydraulic fracture to arrest in its intersection with the natural fracture as signaled as a higher rate of wellbore pressure buildup when the fluid injection rate exceeds the mass rate of fluid entering the fractures.[68]

(2) Constant minimum principal stress

Apparent from Fig. 6 is that a larger maximum principal stress of 13 MPa and with a larger differential stress (III-5) promotes the earlier initiation of the hydraulic fracture and also faster propagation than for the smaller maximum principal stress of 8 MPa and with a smaller differential stress (III-6). The minimum principal stress is maintained at 3 MPa.

Fig. 7 shows that a higher differential stress (III-5) yields a higher fracture pressure than does a smaller differential stress (III-6) at 1200 s for a constant minimum principal stress. This is because normal closure is the dominant response as deviatoric stress increases.[44] For a constant minimum principal stress, a higher maximum principal stress results in a smaller aperture of the natural fractures and promotes a faster and larger pressure buildup in the natural fractures for an identical injection rate (Fig. 6).

In summary of Sections 3.1 and 3.2, higher approach angles and larger stress differences tend to favor fracture crossing – this is due to effective stress transfer across the natural fracture at the tip of hydraulic fracture. In contrast, lower approach angles and smaller stress differences tend to prevent the direct crossing of the hydraulic fracture and arrest the hydraulic fracture as signaled by a more rapid buildup of wellbore pressure.

4.3. *Effect of frictional resistance of natural fractures*

A larger friction coefficient μ of 0.89 favors direct crossing, while a smaller coefficient of friction μ of 0.38 tends to prevent the hydraulic fracture crossing the natural fractures directly (Fig. 8). For the lower friction coefficient this results in the hydraulic fracture reinitiating from the natural fractures where the reinitiation criterion is met. The maximum and minimum principal stresses are 10 MPa and 3 MPa, respectively, and the approach-angle is 60° in this case (Fig. 8).

When the injection rate is held constant, a smaller friction coefficient on the natural fractures allows the enhancement of natural fracture aperture and resulting fluid leak-off, which slows pressure buildup inside the hydraulic fracture. After intersection, the higher and lower friction angle scenarios have visibly different pressure buildup rates. These result from the direct crossing event for the higher coefficient of friction (scenario II-3 as marked by the red arrow at ~180 s in Fig. 8) while the hydraulic fracture in the lower friction coefficient (scenario I-3) is momentarily arrested at the intersection point. Well pressure builds faster for lower coefficient of friction scenario (I-3) as the pump-in rate exceeds the flow rate able to enter the fracture network. Conversely, the hydraulic fracture for the higher friction coefficient scenario (II-3) continues propagating to extend across the natural fractures where increased leak-off reduces pressure build-up in the wellbore.

Therefore, higher frictional strength of the natural fractures

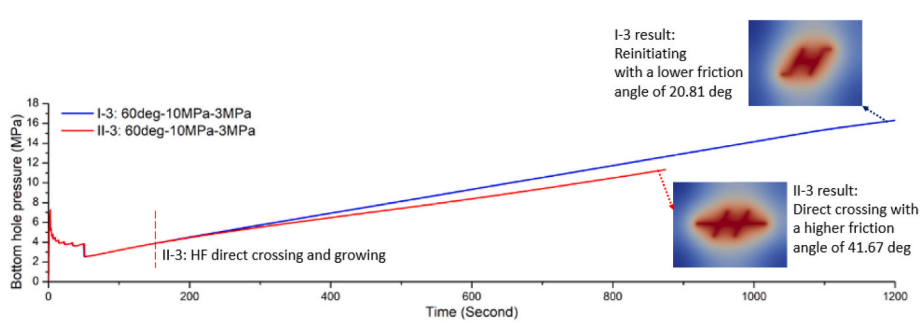

Fig. 8. Bottom hole pressure versus simulation time. Comparison between scenarios for lower friction coefficient (0.38) of natural fractures with reinitiation resulting (I-3) and higher friction coefficient (1.21) of natural fractures with direct crossing resulting (II-3). The applied maximum and minimum principal stresses are 10 MPa and 3 MPa, respectively. The approach-angle is 30°.

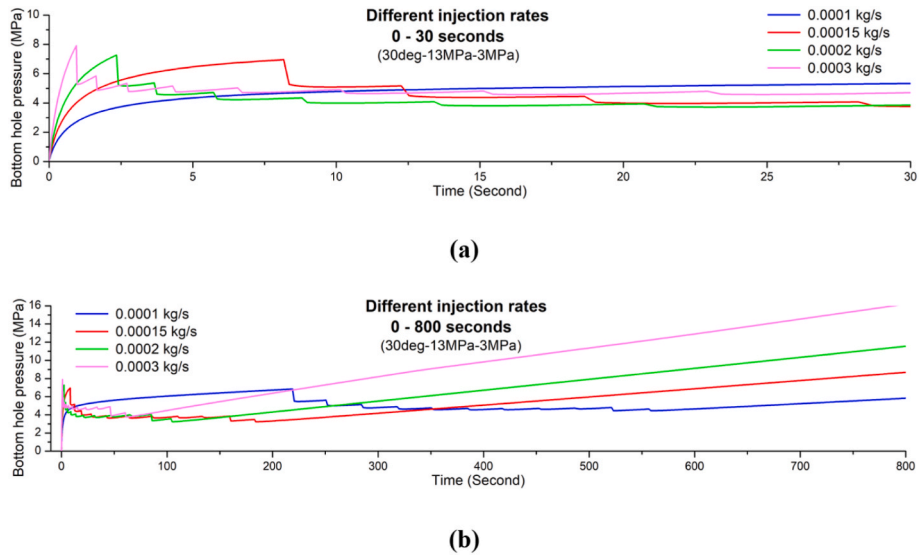

Fig. 9. Bottom hole pressure versus simulation time. Four cases using different constant fluid injection rates (0.0001 kg/s, 0.00015 kg/s, 0.0002 kg/s and 0.0003 kg/s) are compared. The applied maximum and minimum principal stresses are 13 MPa and 3 MPa, respectively. The approach angle is 30°. (a) Zoomed-in details over the first 30 s. (b) Behavior over 0–800 s.

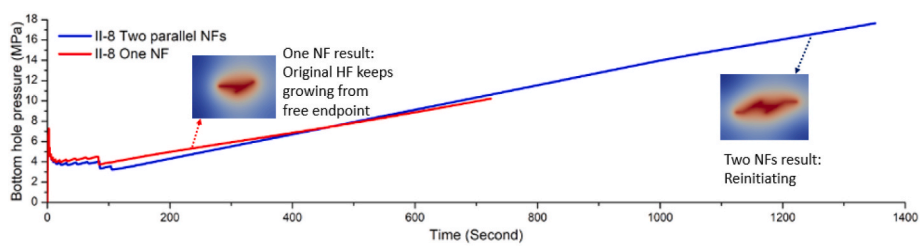

Fig. 10. Bottom hole pressures for each of single and double natural fractures. The applied maximum and minimum principal stresses are 13 MPa and 3 MPa, respectively. The approach-angle is 30°.The single natural fracture promotes hydraulic fracture propagation while the presence of two fractures hinders both propagation and reinitiation.

promotes direct crossing and higher wellbore pressure buildup that has an extending hydraulic fracture which transports more fluid mass away from the wellbore and delays wellbore pressure buildup than in the arrested status.

4.4. Effect of injection rate

Four different constant injection rates of 0.0001 kg/s, 0.00015 kg/s, 0.0002 kg/s and 0.0003 kg/s for the small size model (Fig. 9), are adopted to investigate the effect of the injection rate on pressure evolution during hydraulic fracturing. Fig. 9a zooms-in on the first 30 s s of the simulation and indicates that a larger fluid injection rate triggers earlier and faster hydraulic fracture propagation - the larger injection rate delivers fluid more rapidly to the tip of hydraulic fracture.

After intersection with the natural fracture, the hydraulic fractures remain arrested at the intersection for the duration shown in Fig. 9b. In this period, a larger injection rate increases the pressure buildup at the well (Fig. 9b). The increase in aperture and enhancement in permeability is too small to accommodate all the injectate. As a result, higher injection rates boost fluid mass accumulation at the wellbore, promoting a more rapid buildup in wellbore pressure while propagation is arrested.

In summary, larger injection rates result in the earlier occurrence of hydraulic fracture propagation during the approach to intersection, followed by a higher buildup rate of the wellbore pressure after intersection.

4.5. Effect of multiple natural fractures

The influence of multiple natural fractures on fracture propagation response is explored by comparing cases for both single and double natural fractures. Apparent implication from Fig. 10 is that one tip of the bi-wing hydraulic fracture is arrested by the single natural fracture while the other tip propagates freely in the opposite direction. Conversely, the hydraulic fracture reinitiates from the natural fractures once intersected for the two parallel natural fractures (Fig. 10). For the same duration of the simulation, the total length of the hydraulic fracture interacting with the single natural fracture is greater than that interacting with the two natural fractures.

In addition, the hydraulic fracture propagates at faster velocity and with higher wellbore pressure in single natural fracture than those in the dual natural fractures (Fig. 10). The presence of two natural fractures accommodates greater fluid mass and slows buildup of the wellbore pressure. After intersection, the wellbore pressure for the single natural fracture increases more slowly than for the two natural fractures. This is because the injection rate exceeds the fluid flow rate entering the fractures when the hydraulic fracture is maintained arrested on the two natural fractures. Therefore, natural fracture pattern could influence hydraulic fracture propagation and interaction results with natural fractures via fluid leak-off and redistribution.

4.6. Effect of permeability of natural fracture

The permeability of the natural fracture or fracture network controls

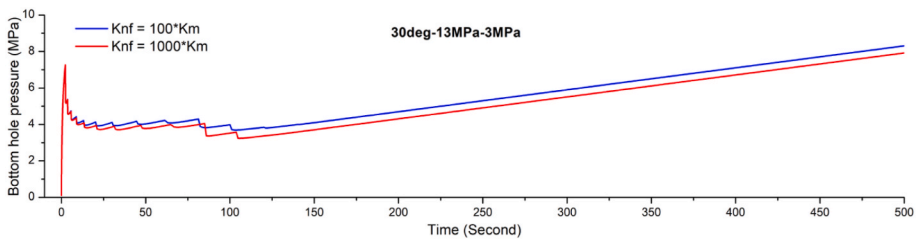

Fig. 11. Evolution of bottom hole pressure with time for two cases with different permeabilities of the natural fracture. Results with the natural fracture one-hundred times (blue) and one-thousand times (red) the permeability of the matrix ($K_m = 1.0 \times 10^{-16} m^2$), respectively. The applied maximum and minimum principal stresses are 13 MPa and 3 MPa, respectively. The approach angle is 30°. (For interpretation of the references to colour in this figure legend, the reader is referred to the Web version of this article.)

the rate of fluid dissipation from induced to natural fractures. Two cases with natural fracture permeability differing by an order of magnitude are used to examine the influence on the borehole pressure. Fig. 11 indicates that hydraulic fracture propagation is slower and with a lower wellbore pressure for a larger natural fracture permeability. This is because more permeable natural fractures promote increase leak-off and reduce the rate of pressure buildup to then activate fracture propagation. Therefore, the hydraulic fracture propagates more slowly and with a lower wellbore pressure when the natural fractures are more permeable. The natural fracture permeability then affects the subsequent evolution of bottom hole pressure.

5. Conclusions

This work presents an investigation and analysis of the key factors that influence hydraulic fracture propagation and interaction with natural fractures with a focus on mechanisms and resulting architecture of the fracture network. This is important in predicting hydraulic fracturing response and evolution of flow paths in fractured rock.

Selected influencing factors include approach-angle, differential stress, coefficient of friction of the natural fractures, injection rate, natural fracture distribution, and the permeability of natural fractures. These parameters capture a broad range of contrasting behaviors and identify the principal mechanisms in conditioning propagation results. Analyses are completed using coupled hydro-mechanical constitutive models in the TOUGHREACT-FLAC3D continuum code.

(1) The conjunctive effects of approach angle and differential stress affect the normal closure response acting on fractures. Larger approach-angles and elevated stress differences favor direct crossing with extensional stresses more readily transferred to the far-side of the approached natural fractures. Otherwise, direct crossing is prohibited when approach angles and stress differences are decreased, with hydraulic fractures arrested by the natural fracture, or arrested and later reinitiating from weak points on the natural fractures if the reinitiation criterion is satisfied.
(2) Triggering of slip or opening of natural fractures is less favored for larger friction coefficients on the natural fracture. This also indicates that higher shear strength favors direct crossing of the natural fracture.
(3) As a hydraulic fracture approaches a natural fracture, larger injection rates result in faster fracture propagation by building pressure more rapidly. Following arrest by the natural fracture, larger injection rates result in higher rates of wellbore pressure buildup when the injection rate exceeds the rate of fluid dissipation into the fractures.
(4) The presence of only a single natural fracture speeds hydraulic fracture propagation with a higher wellbore pressure than for dual natural fractures. This is because a higher density of natural fractures results in increased leak-off, which delays pressure buildup for any given injection rate. In addition, the total length of the hydraulic fracture is greater for a freely extending tip for the presence of a single natural fracture, while the presence of two (or more) parallel natural fractures hinders the propagation of the hydraulic fracture along the same paths with redistributed fluid leak-off and pressure.
(5) When the permeabilities of the natural fractures increase, the hydraulic fracture propagates more slowly with a lower wellbore pressure. Such permeable natural fractures provide effective conduits for the transport and storage of fluid, which reduces the rate of pressure buildup and results in a reduced rate of propagation.
(6) The hydro-mechanical properties of the reservoir play a significant role in modulating the fracture propagation behavior, interaction mechanisms and evolution of flow paths. Hydraulic fracturing is a complex process with this complexity further exacerbated in naturally fractured reservoirs. The foregoing presents a foundation for the rational investigation of the complex evolution of fractured reservoirs using the TOUGHREACT-FLAC3D simulator.

Declaration of competing interest

The authors declare that they have no known competing financial interests or personal relationships that could have appeared to influence the work reported in this paper.

Data availability

The authors do not have permission to share data.

Acknowledgements

This research did not receive any specific grant from funding agencies in the public, commercial, or not-for-profit sectors.

References

1 Valko P, Economides MJ. *Hydraulic Fracture Mechanics*. New York: Wiley; 1995.
2 Blanton TL. *An Experimental Study of Interaction between Hydraulically Induced and Pre-existing Fractures*. Pittsburgh, PA: SPE/DOE Unconventional Gas Recovery Symposium of the Society of Petroleum Engineers; May . SPE/DOE 10847.
3 Blanton TL. *Propagation of Hydraulically and Dynamically Induced Fractures in Naturally Fractured Reservoirs*. Louisville, KY: Unconventional Gas Technology Symposium of the Society of Petroleum Engineers; May . SPE 15261.
4 Warpinski NR, Teufel LW. Influence of geologic discontinuities on hydraulic fracture propagation. *J Petrol Technol*. 1987;39(2):209–220.
5 Gu H, Weng X. *Criterion for Fractures Crossing Frictional Interfaces at Non-orthogonal Angles*. American Rock Mechanics Association; 2010.
6 Renshaw CE, Pollard DD. An experimentally verified criterion for propagation across unbounded frictional interfaces in brittle, linear elastic materials. *Int J Rock Mech Min Sci Geomech Abstr*. 1995;32:237–249.
7 Sarmadivaleh M, Rasouli V. Modified Reinshaw and Pollard criteria for a non-orthogonal cohesive natural interface intersected by an induced fracture. *Rock Mech Rock Eng*. 2014;47:2107–2115.
8 Zhou J, Chen M, Jin Y, Zhang G. Analysis of fracture propagation behavior and fracture geometry using a tri-axial fracturing system in naturally fractured reservoirs. *Int. J. Rock Mech. Min. Sci. Geomech.* 2008;45:1143–1152.
9 Liu Z, Chen M, Zhang G. Analysis of the influence of a natural fracture network on hydraulic fracture propagation in carbonate formations. *Rock Mech Rock Eng*. 2014; 47(2):575–587.
10 Stanchits S, Desroches J, Burghardt J, Surdi A, Whitney N. Rock fabric influence on hydraulic fracture propagation. In: *77th EAGE Conference and Exhibition*. 2015.

11 Zimmerman R, Bodvarsson G. Hydraulic conductivity of rock fractures. *Transport Porous Media*. 1996;23(1):1–30.
12 Jiang D, Sun D, Xiang N, Chen K, Yi H, Ni Z. Lattice Boltzmann numerical simulation and experimental research of dynamic flow in an expansion–contraction microchannel. *Biomicrofluidics*. 2013;7, 034113.
13 Zhao RB, Anderson NL, Rogers JD, Torgashov E. Mapping subsurface seepage flow patterns in proximity to a coal combustion residual landfill using electrical resistivity tomography. *J Geosci Environ Protect*. 2021;9(2):144–157.
14 Snow D. Anisotropic permeability of fractured media. *Water Resour Res*. 1969;5(6): 1273–1289.
15 Mourzenko V, Thovert J, Adler P. Permeability of isotropic and anisotropic fracture networks, from the percolation threshold to very large densities. *Phys Rev E*. 2011;84, 036307.
16 Lin F, Liu C, Zhang P. On a micro-macro model for polymeric fluids near equilibrium. *Pure Appl Math*. 2007;60(6):838–866.
17 Oron AP, Berkowitz B. Flow in rock fractures: the local cubic law assumption reexamined. *Water Resour Res*. 1998;34(11):2811–2825.
18 Brush D, Thomson N. Fluid flow in synthetic rough-walled fractures: Navier-Stokes, Stokes, and local cubic law simulations. *Water Resour Res*. 2003;39(4):1085.
19 Martha LF, Wawrzynek PA, Ingraffea AR. Arbitrary crack representation using solid modeling. *Eng Comput*. 1993;9(2):63–82.
20 Carter BJ, Chen C, Ingraffea AR, Wawrzynek PA. Recent advances in 3D computational fracture mechanics. In: *Ninth International Conference on Fracture*. April 1997. Sydney.
21 Bouchard PO, Bay F, Chastel Y, Tovena I. Crack propagation modelling using an advanced remeshing technique. *Comput Methods Appl Mech Eng*. 2000;189(3): 723–742.
22 Patzak B, Jirasek M. Adaptive resolution of localized damage in quasibrittle materials. *J Eng Mech ASCE*. 2004;130:720–732.
23 Pan PZ, Rutqvist J, Feng XT, Yan F. TOUGH–RDCA modeling of multiple fracture interactions in caprock during CO2 injection into a deep brine aquifer. *Comput Geosci*. 2014;65(0):24–36.
24 Weng X, Kresse O, Cohen C, Wu R, Gu H. Modeling of hydraulic-fracture-network propagation in a naturally fractured formation. *SPE Prod Oper*. 2011;26(4):368-380..
25 Moës N, Dolbow J, Belytschko T. A finite element method for crack growth without remeshing. *Int J Numer Methods Eng*. 1999;46(1):131–150. John Wiley & Sons, Ltd.
26 Lecampion B. An extended finite element method for hydraulic fracture problems. *Int J Num Methods Biomed Eng*. 2009;25(2):121–133.
27 Taleghani AD. *Analysis of Hydraulic Fracture Propagation in Fractured Reservoirs: An Improved Model for the Interaction between Induced and Natural Fractures*. PhD thesis. The University of Texas at Austin; 2009.
28 Li M, Guo P, Stolle DFE, Liang L, Shi Y. *Modeling Hydraulic Fracture in Heterogeneous Rock Materials Using Permeability-Based Hydraulic Fracture Model*. Tongji University and Tongji University Press; 2019.
29 *ABAQUS. ABAQUS Documentation*; 2011. Version 6.10-2.
30 Chen Z. Finite element modelling of viscosity-dominated hydraulic fractures. *J Petrol Sci Eng*. 2012;88–89:136–144.
31 Perkins TK, Kern LR. Widths of hydraulic fractures. *J Petrol Technol*. 1961;13(9): 937–949. SPE-89-PA.
32 Nordgren RP. Propagation of a vertical hydraulic fracture. *SPE J*. 1972;12(4): 306–314. SPE-3009-PA.
33 Khristianovic, Zheltov AK. Formation of vertical fractures by means of highly viscous liquid. In: *4th World Petroleum Congress*. World Petroleum Congress; 1955.
34 Geertsma J, de Klerk F. A rapid method of predicting width and extent of hydraulically induced fractures. *J Petrol Technol*. 1969;21(12):1571–1581.
35 Gan Q, Elsworth D. Analysis of fluid-injection fault reactivation and seismic slip in geothermal reservoirs. *J Geophys Res Solid Earth*. 2014;119:3340–3353.
36 Gan Q, Elsworth D. Thermal drawdown and late-stage seismic-slip fault reactivation in enhanced geothermal reservoirs. *J Geophys Res Solid Earth*. 2014;119:8936–8949.
37 Taron J, Elsworth D. Thermal-hydrologic-mechanical-chemical processes in the evolution of engineered geothermal reservoirs. *Int J Rock Mech Min Sci*. 2009;46: 855–864.
38 Taron J, Elsworth D. Coupled mechanical and chemical processes in engineered geothermal reservoirs with dynamic permeability. *Int J Rock Mech Min Sci*. 2010;47: 1339–1348.
39 Norbeck JH, Mcclure MW, Horne RN. Revisiting stimulation mechanism at fenton hill and an investigation of the influence of fault heterogeneity on the gutenberg-richter b-value for rate-and-state earthquake simulations. In: *PROCEEDINGS Geothermal Reservoir Engineering*. Stanford University; 2016.
40 Li M, Guo P, Stolle D, Li L. Modeling method for a rock matrix with inclusions distributed and hydraulic fracturing characteristics. *J Petrol Sci Eng*. 2017;157: 409–421.
41 Wang W, Gao K, Feng YT. An improved continuum-based finite–discrete element method with intra-element fracturing algorithm. *Comput Methods Appl Mech Eng*. 2021:384.
42 Zhang X, Sanderson D. Fractal structure and deformation of fractured rock masses. In: *Fractals and Dynamic Systems in Geoscience*. Berlin: Springer; 1994:37–52.
43 Cundall PA. A discontinuous future for numerical modelling in geomechanics? *Geotech Eng*. 2001;149:41–47.
44 Gan Q, Elsworth D. A continuum model for coupled stress and fluid flow in discrete fracture networks. *Geomech Geophys Geo-energ Geo-resour*. 2016;2:43–61.
45 Min KB, Jing L. Numerical determination of the equivalent elastic compliance tensor for fractured rock masses using the distinct element method. *Int J Rock Mech Min Sci*. 2003;40(6):795–816.
46 Hu Y, Gan Q, Hurst A, Elsworth D. Hydraulic fracture propagation and interaction with natural fractures by coupled hydro-mechanical modeling. *Geomech Geophys Geo-energ Geo-resour*. 2022;8:4. https://doi.org/10.1007/s40948-021-00307-9.
47 Xu T, Spycher N, Sonnenthal E, Zheng L, Pruess K. *TOUGHREACT User's Guide: A Simulation Program for Non-isothermal Multiphase Reactive Transport in Variable Saturated Geologic Media, Version 2.0. Technical Report LBNL-DRAFT*. Lawrence Berkeley National Laboratory (LBNL); 2012:240.
48 Itasca Consulting Group. *Inc. FLAC3D. Fast Lagrangian Analysis of Continua in Three-Dimensions, Ver. 5.0*. Minneapolis: Itasca; 2000.
49 Segall P. Rate-dependent extensional deformation resulting from crack growth in rock. *J Geophys Res*. 1984;89-B6:4185–4195.
50 Atkinson BK, Meredith PG. Experimental fracture mechanics data for rocks and minerals. In: Atkinson BK, ed. *Fracture Mechanics of Rock*. London: Academic Press; 1987:477–525.
51 Olson JE. Joint pattern development: effects of subcritical crack-growth and mechanical crack interaction. *J Geophys Res*. 1993;98:12251–12265.
52 Atkinson BK. Subcritical crack-growth in geological-materials. *J Geophys Res*. 1984; 89:4077–4114.
54 Biot MA. General theory of three-dimensional consolidation. *J Appl Phys*. 1941;12: 155–164.
55 Biot MA. Theory of propagation of elastic waves in a fluid-saturated porous solid, I, Low-frequency range. *J Acoust Soc Am*. 1956;28(2):168–178.
56 Biot MA. Theory of propagation of elastic waves in a fluid-saturated porous solid, II, Higher-frequency range. *J Acoust Soc Am*. 1956;28(2):179–191.
57 Biot MA. Mechanics of deformation and acoustic propagation in porous media. *J Appl Phys*. 1962;33(4):1482–1498.
58 Taron J. *Geophysical and Geochemical Analyses of Flow and Deformation in Fractured Rock*. The Pennsylvania State University. PhD thesis; 2009.
59 Biot MA, Willis DG. The elastic coefficients of the theory of consolidation. *J Appl Mech*. 1957;24:594–601.
60 Khaled MY, Beskos DE, Aifantis EC. On the theory of consolidation with double porosity, III, A finite element formulation. *Int J Numer Anal Methods GeoMech*. 1984;8 (2):101–123.
61 Warren JE, Root PJ. The behavior of naturally fractured reservoirs. *Soc Petrol Eng J*. 1963;3:245–255.
62 Zimmerman R, Chen G, Bodvarsson G. A dual-porosity reservoir model with an improved coupling term. In: *Proceedings of the 17th Workshop on Geothermal Reservoir Engineering*. 1992. Stanford, Ca.
63 Zhou J, Zhang L, Pan Z, Han Z. Numerical studies of interactions between hydraulic and natural fractures by Smooth Joint Model. *J Nat Gas Sci Eng*. 2017;46:592–602.
64 Zhou J, Zhang L, Braun A, Han Z. Investigation of processes of interaction between hydraulic and natural fractures by PFC modeling comparing against laboratory experiments and analytical models. *Energies*. 2017;10(7),1001..
65 Wan T, Yu Y, Sheng JJ. Experimental and numerical study of the EOR potential in liquid-rich shales by cyclic gas injection. *J. Unconv. Oil Gas Resour*. 2015;12:56–67.
66 Zhang J, Yin S. A three-dimensional solution of hydraulic fracture width for wellbore strengthening applications. *Petrol Sci*. 2019;16:808–815.
67 Chen FY, Zhou SW, Zhuang XY, Zhang WG. Phase field modelling of a single horizontal fluid-driven fracture propagation in spatially variable rock mass. *Int J Comput Methods*. 2020, 022034.
68 Lecampion B, Desroches J, Jeffrey RG, Bumger AP. Experiments versus theory for the initiation and propagation of radial hydraulic fractures in low-permeability materials. *J Geophys Res Solid Earth*. 2017;122:1239–1263.